Predicting the High Angle of Attack Characteristics of a Delta Wing at Low Speed

Sabet Seraj* and Joaquim R. R. A. Martins[†]
University of Michigan, Ann Arbor, Michigan 48109

Ensuring the safe operation of new supersonic transport aircraft requires understanding their stability during takeoff and landing. These phases involve flying at subsonic speeds and high angles of attack, where the aerodynamics are characterized by unsteady vortical flow. In this work, we assess the accuracy of Reynolds-averaged Navier–Stokes (RANS) and delayed detached eddy simulations (DDES) at these flow conditions. We use a delta wing with an aspect ratio of 2 as a simplified representation of a supersonic transport wing and compare the predicted force and moment coefficients to experimental data for angles of attack from 0 to 40 degrees. We formulate a steadiness metric to distinguish between steady and unsteady angles of attack. We find that RANS accurately predicts vortex effects in the steady regime but is inaccurate at high angles of attack where the flow is unsteady. DDES is more reliable in the unsteady regime, but the computational cost is at least 100 times that of RANS. Predicting the pitching moment at the highest angles of attack is difficult even with DDES on a 69 million cell mesh. These results provide guidelines for choosing the appropriate fidelity depending on the flow characteristics, the required accuracy, and the computational budget.

I. Introduction

Supersonic transport (SST) aircraft commonly use thin, highly swept wings to reduce supersonic wave drag. This design decision also influences the aircraft's low-speed aerodynamic characteristics, particularly during takeoff and landing when the aircraft is flying at high angles of attack. The flow over highly swept wings at high angles of attack is unsteady, separated, and characterized by leading edge vortices [1]. Leading edge vortices can be advantageous in some cases. The Concorde relied on leading edge vortices instead of high-lift devices to generate lift during subsonic flight [2]. On the other hand, these vortices can contribute to unstable pitch-up behavior at moderate to high angles of attack [3], conditions that fall within the aircraft's flight envelope. Accurately predicting high angle of attack aerodynamics is essential to designing the next generation of SSTs.

Historically, numerical methods for low-speed analysis of supersonic aircraft has involved vortex lattice methods (VLMs) with empirical corrections for vortex lift, vortex breakdown, or other nonlinearities [4–6]. Some of the corrections were based on prior theoretical models [7–9], whereas others were developed specifically for the method. The shortcoming of these methods is that their predictive capability is limited. This can be a result of the experimental data used to construct empirical models, the selection of model parameters, or the generality of the model itself. For example, Lan and Hsu [4] constructed a vortex breakdown model using a least squares fit of delta wing experimental data. The approximate nature of this fit caused the vortex breakdown behavior of a 70 deg delta wing to be incorrectly modeled as a cross between 60 and 80 deg wings. Another example is the pitch-up estimation model developed by Benoliel and Mason [6]. Whereas, the model accurately predicted pitch-up caused by outboard separation, it was less reliable for vortex dominated pitch-up cases. In addition, the model required the user to specify maximum sectional lift coefficients prior to the analysis, limiting the model's usefulness for design exploration.

VLM-type methods remain an important tool for rapid design analysis. However, more recent work has also turned to high fidelity computational fluid dynamics (CFD) to resolve the underlying physics rather than model them. Numerous papers have dealt with CFD for delta wings or similar supersonic wing geometries. We focus on validation studies for unsteady turbulent flows because these are the most relevant for our purposes. The first three papers we mention study a 70 deg delta wing at an angle of attack of 27 deg. This is a popular validation case because of the full field experimental data collected by Mitchell et al. [10]. Soemarwoto and Boelens [11] used unsteady Reynolds-averaged Navier–Stokes (unsteady RANS or URANS) to study this case. They found that accuracy was hindered by a lack of mesh density and the inability of URANS to model short time-scale unsteadiness. They suggested that large eddy simulation (LES)

---

or a hybrid RANS/LES method could provide more accurate results. Görtz [12] used a hybrid RANS/LES method called detached eddy simulation (DES) for the same case. They found that sufficiently refined results were accurate but that the unsteady vortex effects were sensitive to both the mesh density and the time step. Morton [13] also used DES and found the solution to be mesh sensitive. They showed that adaptive mesh refinement could be used to reduce the computational cost.

There has been some CFD work for realistic supersonic configurations at high angles of attack and flight Reynolds numbers. The F-16XL aircraft was the subject of the Cranked-Arrow Wing Aerodynamics Project, International (CAWAPI) [14]. CAWAPI researchers compared high-fidelity CFD predictions to F-16XL flight test data, including one subsonic case at an angle of attack of 19.8 deg. We highlight two studies on this flight condition. The first by Lofthouse and Cummings [15] showed that delayed detached eddy simulation (DDES) combined with large meshes could accurately match the flight test data. The second study by Tomac et al. [16] compared the results from RANS, URANS, and hybrid RANS/LES models. They found that steady RANS matched the experimental pressure distributions at parts of the wing where the flow was steady. The unsteady models matched the flight test data more consistently. They noted that RANS was reasonably accurate because the flight condition exhibited only "moderate unsteady aerodynamics". In a separate work, Forsythe et al. [17] considered the F-15E aircraft at an angle of attack of 65 deg. The flow regime in this case is unlike any of the studies described above. The angle of attack is well past stall and leading edge vortex effects are diminished. The authors found that RANS and DES predictions were both within 10% of flight test data, with DES being slightly more accurate. They also reported that the forces were not particularly sensitive to mesh refinement.

All of the studies mentioned above deal with a single angle of attack. There are far fewer validation studies at multiple angles of attack, possibly because of the increased computational cost or a lack of experimental data. One such study by Cummings and Schütte [18] used RANS and hybrid RANS/LES models to simulate the flow over a 65 deg delta wing at angles of attack of 13.3, 18.4, and 23 deg. However, the flow was mostly steady even at the highest angle of attack. As a result, they found that RANS was similarly accurate to the best hybrid RANS/LES model. Another study by Jeans et al. [19] found that DDES provides accurate force and moment values for a generic fighter configuration at angles of attack between 15 and 40 deg. However, they did not show any solutions between 30 and 40 deg where the breaks in the force and moment coefficients occur. It is unclear whether DDES captures this trend correctly.

Our objective is to investigate how accurate RANS and DDES models are at predicting the low-speed aerodynamics of a delta wing at angles of attack up to and past stall. We are particularly interested in capturing the trends in the force and moment coefficients at high angles of attack because these are important for the low-speed stability of SSTs. This is similar to the approach taken by the High Lift Prediction Workshop [20] for conventional transonic wings.

We choose to work with a delta wing for three reasons. First, delta wings are often the starting point for SST wing designs. Second, the geometry is relatively simple to generate and mesh. Lastly, experimental force and moment coefficients across a range of angle of attack are available for our chosen geometry. We further discuss the geometry and flow conditions in Sec. II. We then present RANS and DDES results in Sec. III and Sec. IV, respectively.
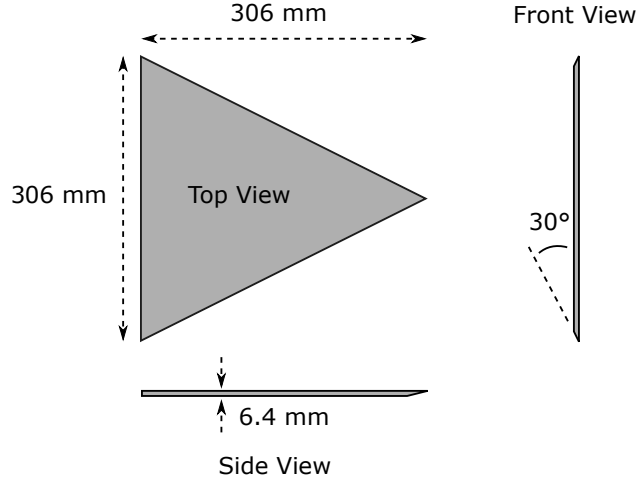
II. Delta Wing Geometry and Flow Conditions

The delta wing geometry and flow conditions are based on the experimental configuration of Jarrah and Ashley [21]. We choose to work with a delta wing with an aspect ratio of 2, which corresponds to a leading edge sweep of 63.4 deg. This is representative of a typical SST wing sweep. For comparison, the Concorde had an average leading edge sweep of 60 deg [2]. The delta wing (Fig. 1) is a flat plate with a sharp leading edge and a blunt trailing edge. The leading edge cut angle is 30 deg. The root chord length is 306 mm, and the thickness is 6.4 mm. We give the geometry a 0.5 mm radius of curvature at all edges to avoid mesh quality issues at infinitely sharp corners. We assume that this is within the manufacturing tolerances of the experimental configuration.

The Reynolds number based on the root chord length is 590 000. We assume standard sea level conditions for the rest of the flow properties because they are not specified in the experimental paper. The Mach number under this assumption is 0.083. We compare RANS and DDES simulations against the experimental lift, drag, and pitching moment coefficients at angles of attack from 0 to 40 deg at 5 deg increments. This range of angle of attack includes the point of maximum lift and the break in the lift and moment curves that follow immediately afterwards. Table 1 lists the reference quantities and flow conditions. The reference chord is only used in nondimensionalizing the pitching moment. The listed reference area is for the full wing. We use a half-span wing with a symmetry plane at the root for all simulations.

The reference point for the pitching moment warrants further discussion because it is most likely reported incorrectly in the experimental paper. In Jarrah and Ashley [21], the pitching moment is defined as positive nose up about a point

77% of the root chord aft of the apex. We instead take the correct definition to be positive nose down about a point 23% of the root chord in front of the apex. This results in a physically realistic interpretation of the experimental values and is further justified by the computational results shown in the remainder of this work.

Fig. 1 Delta wing geometry based on the experimental configuration of Jarrah and Ashley [21]

Table 1 Reference quantities and flow conditions

Quantity	Value
Root chord (L_{ref})	0.306 m
Reference chord	0.204 m
Reference area	0.046818 m^2
Freestream velocity (U_∞)	28.16 m/s
Reynolds number	590 000
Mach number	0.083

III. RANS Simulations Using ADflow

ADflow [22] is a second-order finite volume flow solver for multiblock and overset structured meshes. We use ADflow to solve the steady, compressible RANS equations with the standard Spalart–Allmaras turbulence model [23]. We use the Jameson–Schmidt–Turkel scheme with scalar dissipation [24] for inviscid fluxes and central differencing for viscous fluxes. All solutions are converged to a total residual norm of 10^{-8} relative to the freestream residual. Using the approximate Newton–Krylov startup strategy [25] in ADflow allows us to efficiently converge highly separated flows to a steady solution. Although we expect RANS to be inaccurate at high angles of attack where unsteady effects are important, we use ADflow to determine the regime where RANS results are valid and how large the errors are outside of this regime.

A. Mesh Convergence Study

We use two different mesh types with ADflow. The first is a multiblock mesh (Fig. 2a). We generate the mesh in two steps. First, we create a multiblock surface mesh manually using Ansys ICEM CFD. We then extrude the surface mesh to generate a volume mesh using pyHyp [26], a hyperbolic mesh generation code based on the work of Chan and Steger [27]. The second mesh type is an overset mesh (Fig. 2b). We march the same multiblock surface mesh out a small distance (highlighted in blue in the figure) and embed this mesh in a background mesh. The background mesh has a Cartesian refinement region near the wing and is surrounded by a hyperbolic O-mesh. Using an overset mesh allows

3

us to take advantage of the high quality boundary layer cells produced by hyperbolic meshing and control the refinement in the separated flow region using Cartesian meshing. For all meshes, the farfield boundary is 20 times the root chord length away from the delta wing surface.

(a) Multiblock mesh (M1)
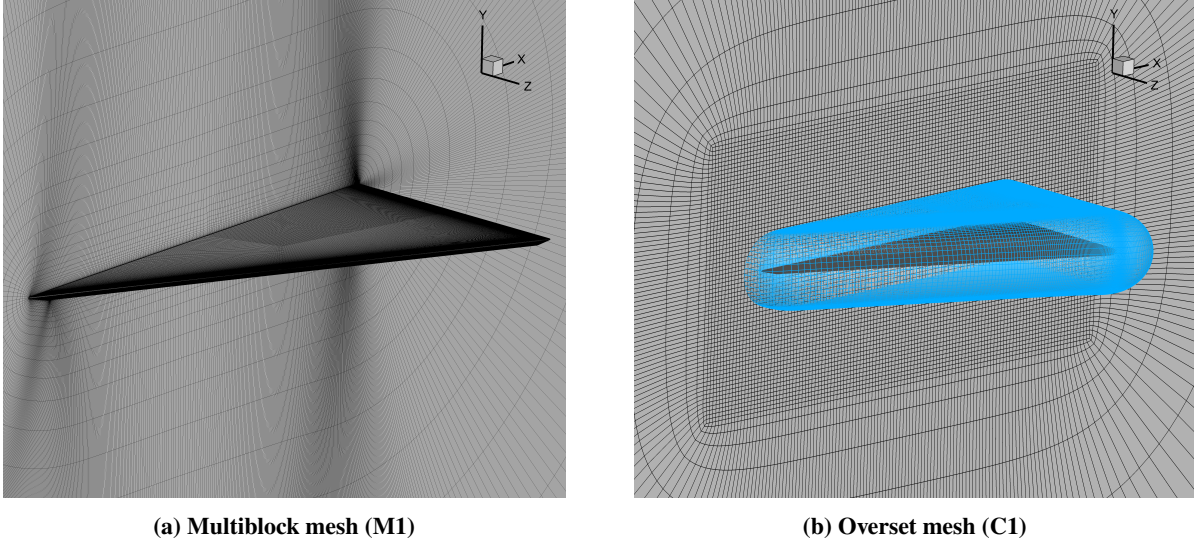
(b) Overset mesh (C1)

Fig. 2   RANS meshes

We generate two mesh families by uniformly coarsening the finest mesh, twice for the multiblock mesh and once for the overset mesh. Table 2 lists the characteristics for each mesh. The number of cells for the overset meshes is the number of compute cells after implicit hole cutting [28]. We use these meshes to run a mesh convergence study. We choose an angle of attack of 5 deg for the study because we expect RANS to resolve the physics at this condition and consequently converge to a realistic solution as the mesh is refined. Figure 3 shows the results of the study. We also report the maximum y^+ from the mesh convergence solutions in Table 2. The extrapolated drag values differ by 2 counts, suggesting that the multiblock and overset meshes will converge to nearly the same solution. The overset meshes provide closer to mesh-converged results with a smaller number of cells than the multiblock meshes. This is because the overset mesh has more effective local refinement, particularly in the off-wall direction.

Table 2   RANS mesh characteristics

Mesh type	Label	Cells (N)	y^+_{max}
Multiblock	M0	65 458 176	0.62
	M1	8 182 272	1.29
	M2	1 022 784	2.56
Overset	C0	15 867 929	1.22
	C1	1 948 651	1.88

B. Angle of Attack Sweep

Figure 4 shows RANS results for angles of attack from 0 to 40 deg. We use both multiblock and overset meshes. Based on the mesh convergence study in Sec. III.A, we use the M1 and C1 meshes to balance accuracy and computational cost. The aerodynamic coefficients match the experimental data well up to 20 deg. We show in Sec. IV.C that this corresponds to the steady regime. The main advantage of using the overset mesh is better prediction of the lift at 15 and 20 deg. However, the pitching moment at 20 deg is less accurate than the multiblock solution. The accuracy of RANS drops off sharply once the flow is unsteady. The lift and drag are underpredicted by 10–20% because RANS does not resolve the forces generated by unsteady vortex effects. In addition, the break in the pitching moment is not captured.

4
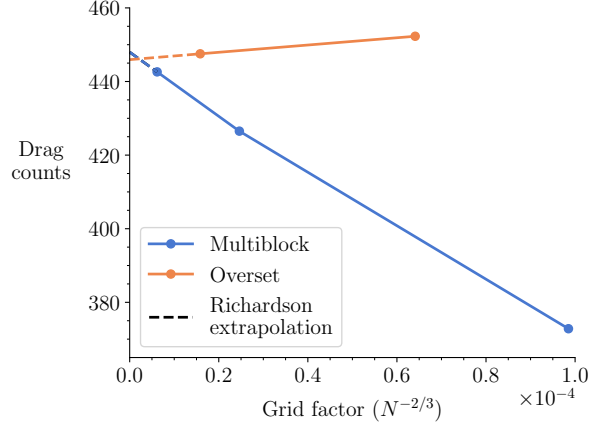
Fig. 3   RANS mesh convergence at $\alpha = 5°$

To visualize the RANS results in the steady regime, we plot the upper surface pressure coefficient and streamlines in Fig. 5. The leading edge vortex strength increases with angle of attack. In addition, the flow moves increasingly in the spanwise direction as the angle of attack increases. This corresponds to the primary reattachment line moving closer to the wing root, indicating that the leading edge vortex is becoming larger. RANS can resolve these large-scale vortices if the flow is steady. This was also discussed by Cummings and Schütte [18].

IV. DDES Using pimpleFoam

For DDES, we use pimpleFoam, a time-accurate, incompressible finite volume flow solver that is part of the OpenFOAM toolbox [29]. An incompressible solver is a reasonable choice because we expect that the low freestream Mach number will result in minimal compressibility effects. We use the SA-DDES formulation [30], a hybrid RANS/LES model that uses the Spalart–Allmaras turbulence model near the wall and a subgrid scale model away from the wall. We use the second-order backward difference in time, the Beam–Warming scheme [31] for inviscid fluxes, and central differencing for viscous fluxes. The resulting discretization is second-order accurate in time and space.

The PIMPLE algorithm used by pimpleFoam is an extension of the PISO algorithm [32]. The most widely used version of the PISO algorithm solves the discretized equations at each time step by performing a velocity predictor step followed by two pressure corrector steps. The PIMPLE algorithm loops over this entire iteration process multiple times at each time step. This enables the use of larger time steps. Each iteration of the outermost loop is termed an outer corrector iteration. Unless otherwise stated, we use one outer corrector iteration, which is equivalent to the PISO algorithm. However, using pimpleFoam lets us test for outer loop convergence, which we discuss in Sec. IV.A.

A. Convergence Studies

Assessing what constitutes a converged solution is more involved for DDES than for RANS. For DDES, we must consider both spatial and temporal discretization errors. We also look at pimpleFoam's iterative convergence. We use an angle of attack of 25 deg for all convergence studies in this section for two reasons. First, we expect DDES to be accurate and convergent at this condition. Second, this condition should be unsteady and thus provide convergence information that is applicable to unsteady cases.

Figure 6 shows the unstructured meshes that we use with pimpleFoam. We use the cfMesh library to generate Cartesian meshes with nested refinement zones and boundary layer cells at the wing surface. Table 3 lists the cell counts for each mesh and the maximum y^+ values from the mesh convergence study discussed later in this section. The 69M mesh is a nearly uniform refinement of the 12M mesh outside of the boundary layer region. The number of boundary layer cells is the same for both meshes, which is why the 69M mesh has only 5.6 times the number of cells rather than 8 times. The 24M mesh adds local refinement to the 12M mesh in the separated flow region near the wing as a compromise between the 12M and 69M meshes. The farfield boundary for all meshes is 20 times the root chord length away from the delta wing surface.
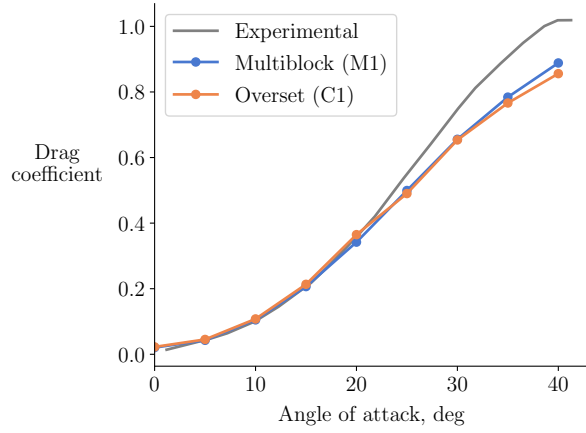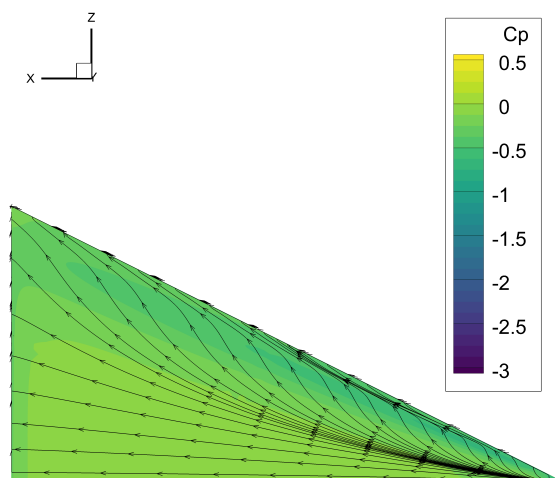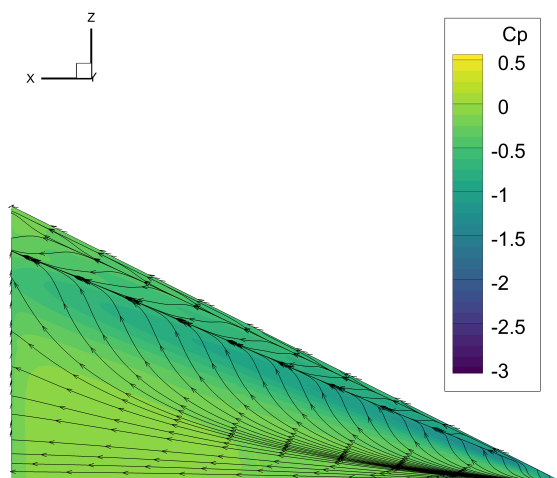
(a) Drag
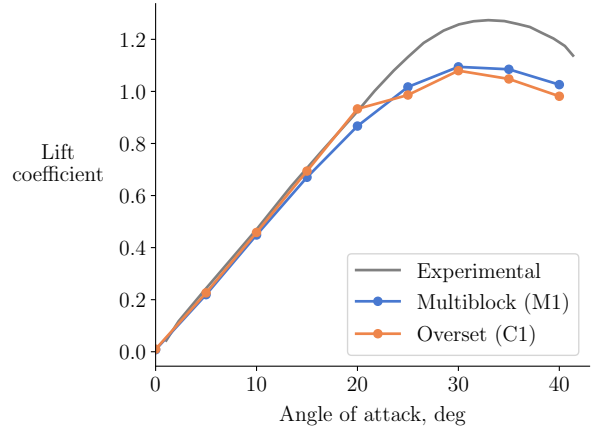
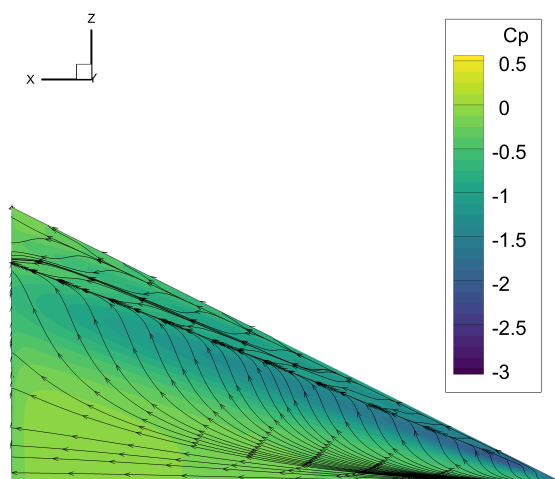
(b) Lift
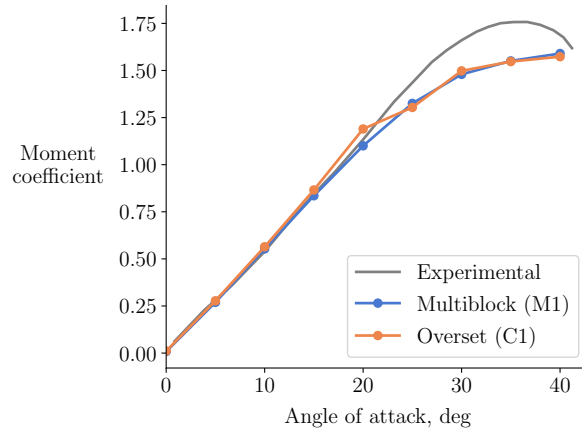
(c) Pitching moment

Fig. 4   Comparison of RANS force and moment coefficients with experimental data from [21]

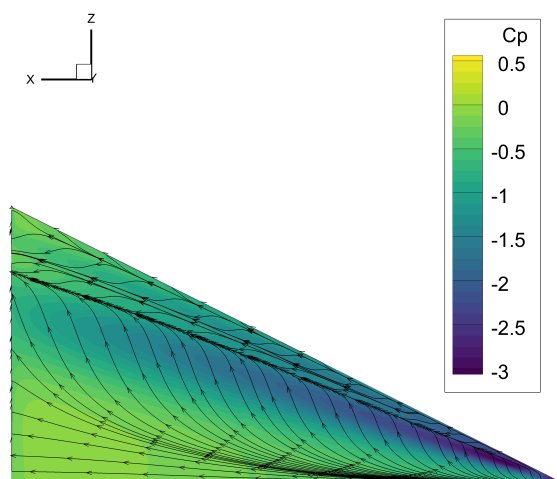**(a)** $\alpha = 5°$

(b) $\alpha = 10°$

(c) $\alpha = 15°$

(d) $\alpha = 20°$

Fig. 5   RANS (C1) upper surface pressure coefficient contours and streamlines

We start by running a time step refinement study with the coarsest (12M) mesh. Ashton et al. [33] suggest that choosing the time step such that the Courant number is less than one in the LES regions provides suitable accuracy for DDES. This equates to a time step of 1.4×10^{-4} s for the 12M mesh. Based on this rule of thumb, we conduct a time step refinement study with time steps ranging from 2×10^{-4} s to 2.5×10^{-5} s. The force and moment coefficients change less than 1% when refining the time step from 5×10^{-5} s to 2.5×10^{-5} s (Fig. 7a). Based on this, we use a time step of 5×10^{-5} s for all subsequent results. Running a mesh convergence study shows that the coefficients change less than 1% from the 24M mesh to the 69M mesh (Fig. 7b). This suggests that the 24M mesh should be sufficiently fine for angles of attack up to at least 25 deg.

Lastly, we check for convergence with the number of outer corrector iterations. Because we are not enforcing a residual tolerance at each time step, it is important to verify that the solution is independent of the iteration settings. The computational cost scales linearly with the number of outer corrector iterations. As a result, we use the 12M mesh to reduce the computational cost of this study. The number of outer corrector iterations has a negligible effect on the coefficients (Fig. 7c). This justifies using only one iteration. We expect similar levels of convergence for the more refined meshes because the outer loop convergence is mainly dependent on the Courant number. With a time step of 5×10^{-5} s, the Courant number in the LES region is less than one for all meshes.

Table 3   DDES mesh characteristics

| Label	Cells (N)	$y^+_{\max}$
69M	69 167 178	0.49
24M	24 481 833	1.24
12M	12 281 039	1.24

B. Angle of Attack Sweep

We run DDES with the 24M mesh for angles of attack from 0 to 40 deg. From 25 to 40 deg, we also run DDES with the 69M mesh because these are the most challenging flow conditions to accurately resolve. The aerodynamics near the point of maximum lift are dominated by unsteady vortex effects, such as vortex breakdown [1]. Figure 8 shows how vortex breakdown causes the vortex structure to become progressively less coherent as the angle of attack increases and the vortex breakdown location moves closer to the apex.

The predicted coefficient values match the experimental data well up to 25 deg (Fig. 9). There are some discrepancies at higher angles of attack. The lift and drag at 30 deg are underpredicted by 4–6%. Refining the mesh from 24M to 69M does not improve the accuracy at this condition. This suggests that the DDES model does not fully resolve the unsteady vortex effects near the point of maximum vortex strength. The 40 deg condition is the most sensitive to mesh refinement. The 69M mesh correctly predicts that there is a break in the pitching moment between 35 and 40 deg, whereas the 24M mesh does not. The suction predicted by the 69M mesh at 40 deg is lower and more localized near the wing apex compared to the 24M mesh (Fig. 10). This results in lower lift and drag, less pitch-down moment, and a better match with the experimental data. However, DDES does not fully capture the shape of the experimental pitching moment curve from 30 to 40 deg even with the 69M mesh.

DDES is computationally expensive. Using 320 Skylake cores on NASA's Electra supercomputer, the 40 deg case takes approximately 24 and 81 hours to run with the 24M and 69M meshes, respectively. This is approximately 100–1000 times more expensive than RANS in terms of total CPU time. This comparison is meant to be an order of magnitude estimate, and we acknowledge that there are many differences between the RANS and DDES solvers that contribute to the cost disparity.

C. Time Series Analysis

We now describe how we compute force and moment coefficient values from DDES time histories. We initialize the flow from freestream conditions and run each DDES case for 2.0 seconds in simulation time. We then compute the coefficients as the time-average from 0.5 to 2.0 seconds to avoid including the transients at the start of the simulation. Figure 11 shows the time histories and cumulative mean of the moment coefficient for a few representative cases. We find that with this averaging window, the cumulative mean flattens out by the end of the simulation for all but one case.
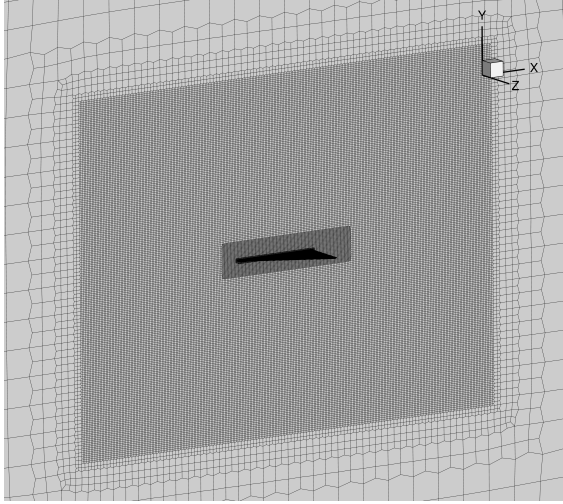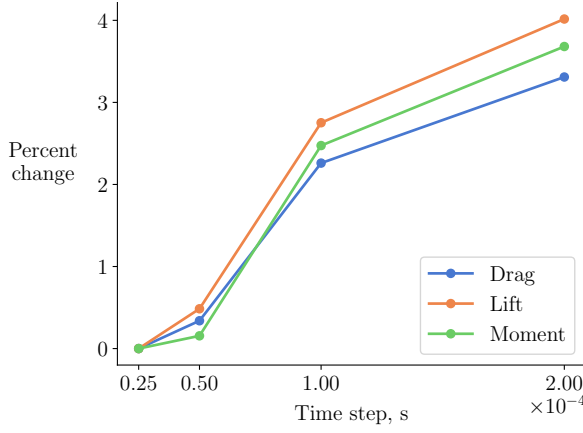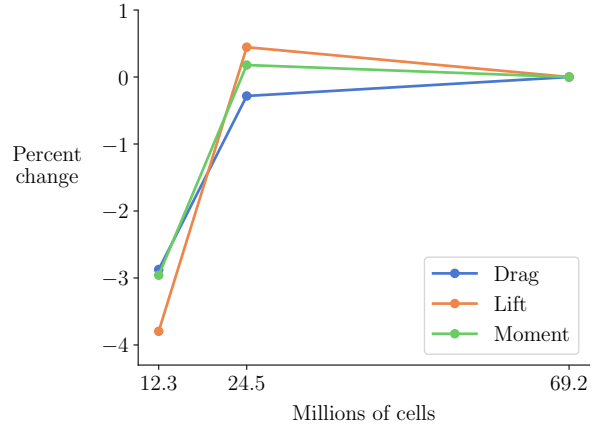
(a) 12M
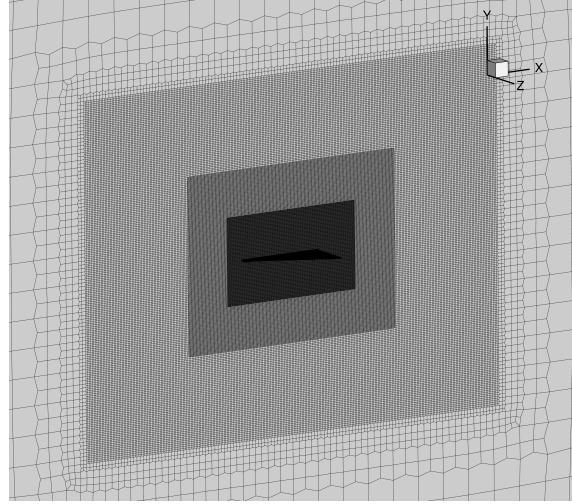
(b) 24M
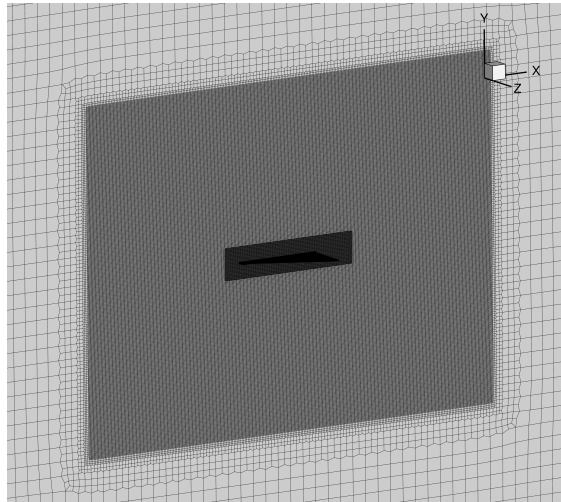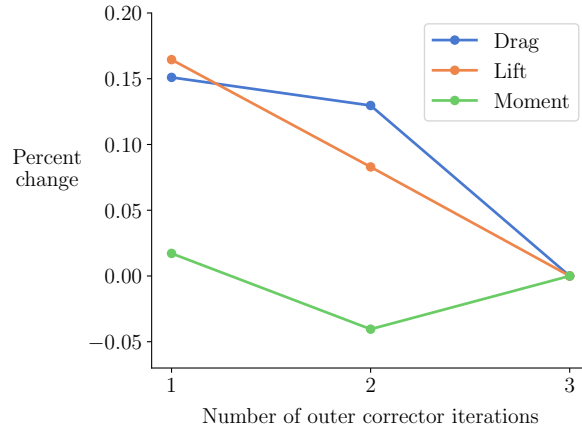
(c) 69M

Fig. 6   DDES meshes

(a) Time step refinement with 12M mesh

(b) Mesh refinement with $\Delta t = 5 \times 10^{-5}$ s

(c) Outer loop convergence for 12M mesh, $\Delta t = 5 \times 10^{-5}$ s

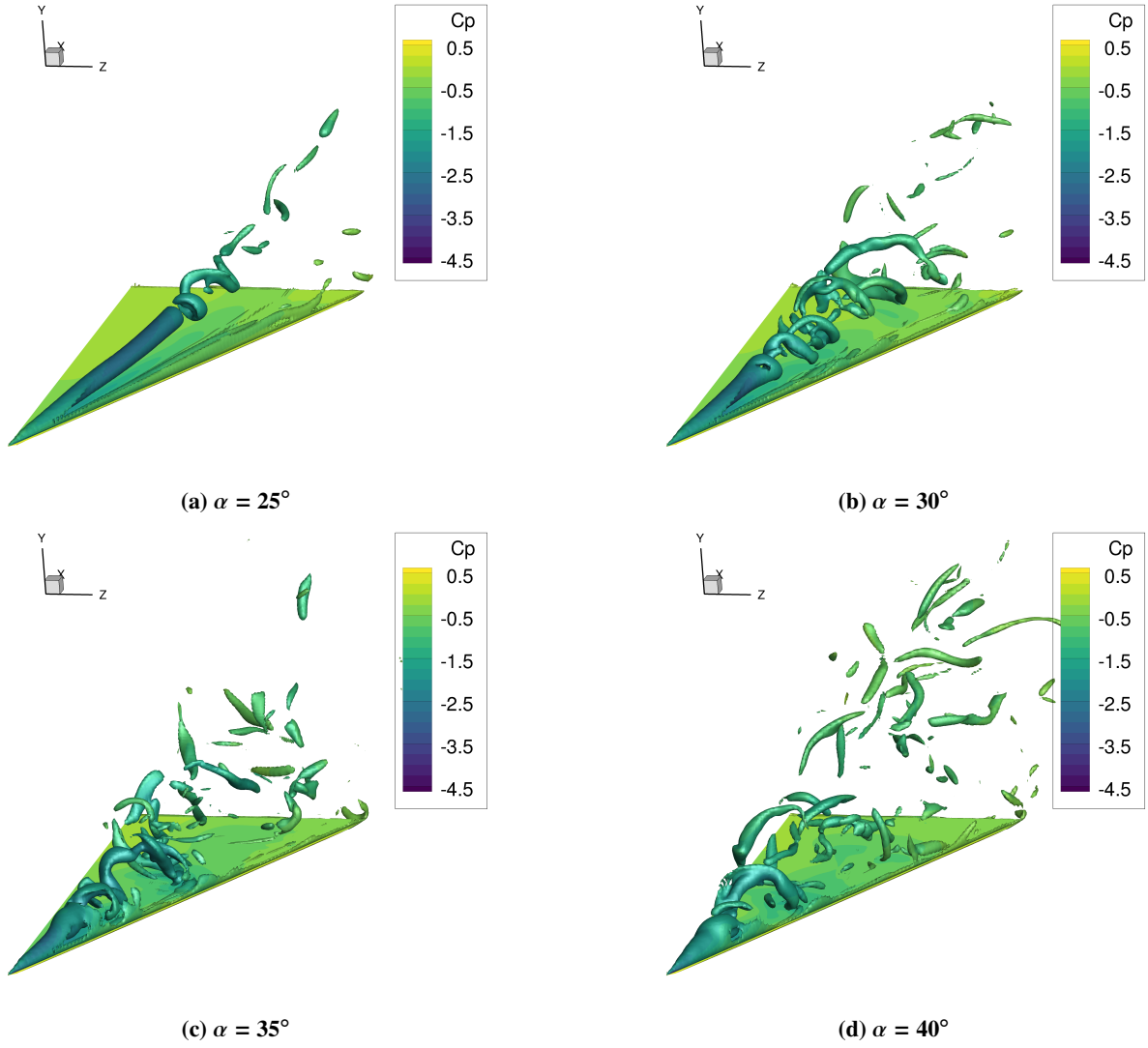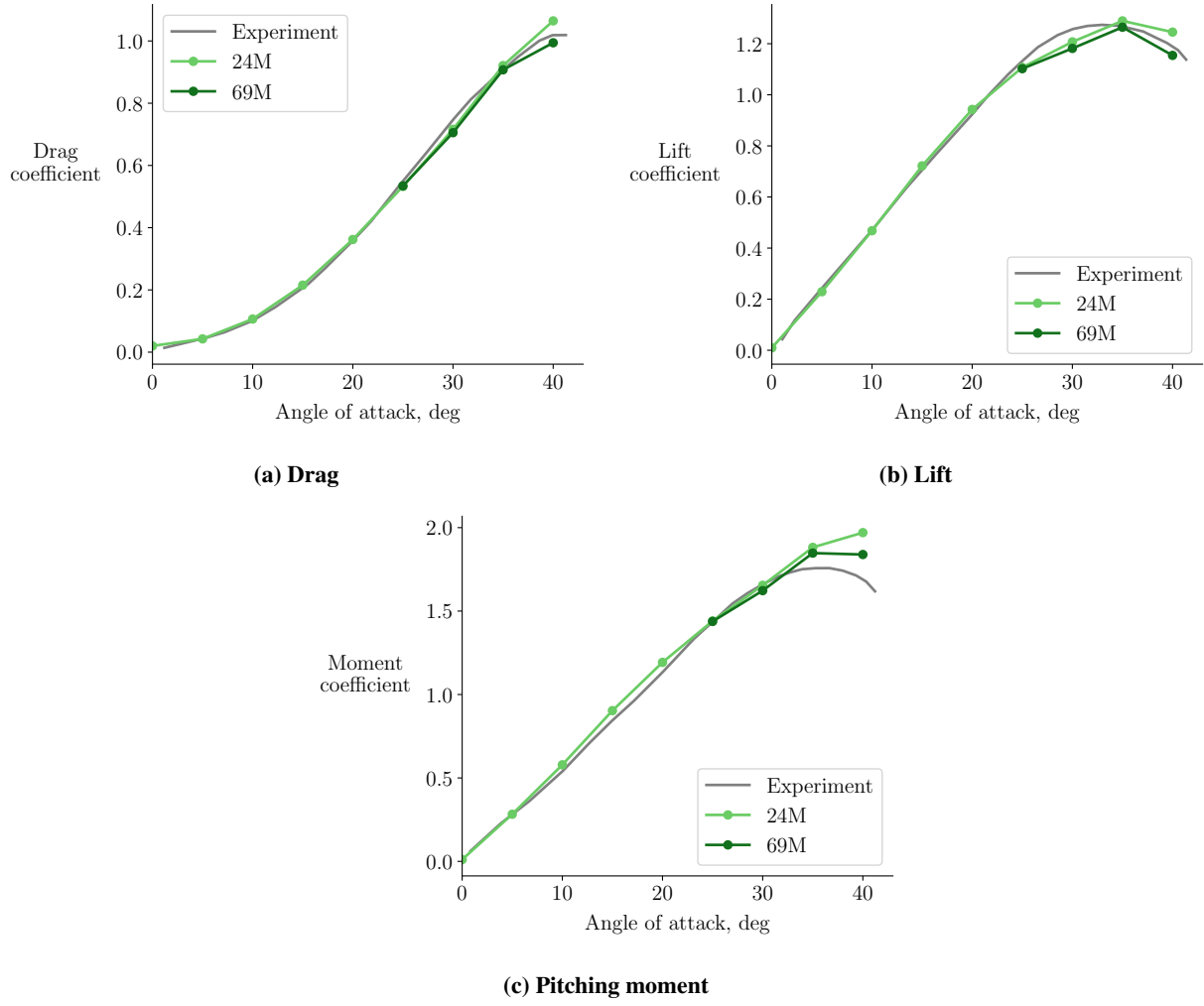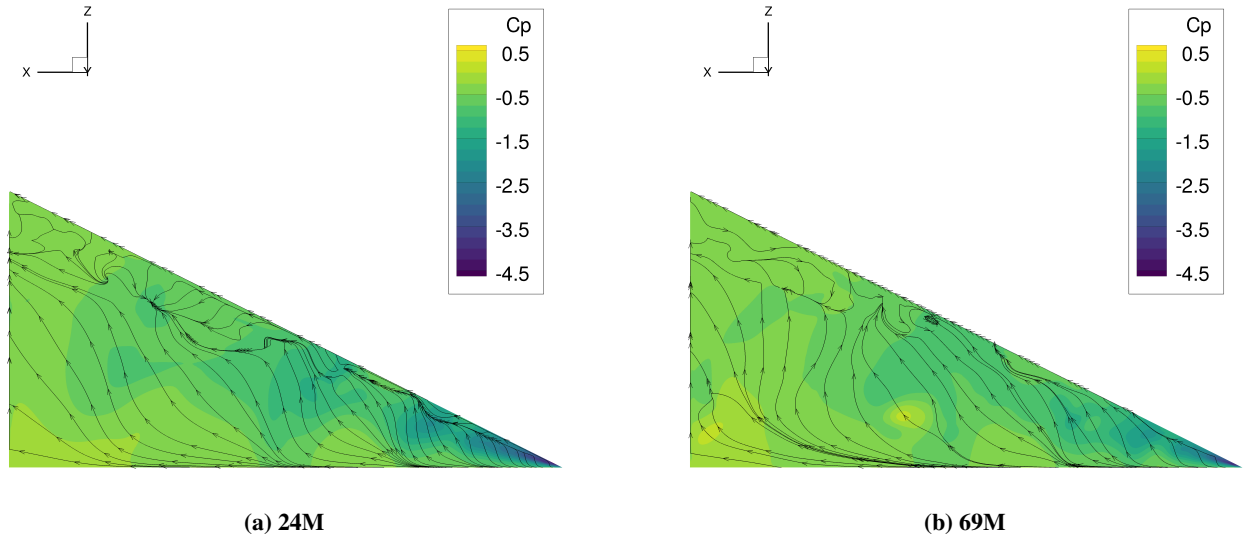**Fig. 7   DDES convergence with discretization and solver parameters at $\alpha = 25°$**

(a) $\alpha = 25°$

(b) $\alpha = 30°$

(c) $\alpha = 35°$

(d) $\alpha = 40°$

Fig. 8　DDES (24M) Q-criterion isosurfaces for $Q = 10^7$ at $t = 1.2\,\mathrm{s}$

(a) Drag

(b) Lift

(c) Pitching moment

Fig. 9   Comparison of DDES force and moment coefficients with experimental data from [21]


(a) 24M

(b) 69M

Fig. 10   DDES upper surface pressure coefficient contours and streamlines for $\alpha = 40°$ at $t = 1.2\,\text{s}$

For the 40 deg case with the 69M mesh, the cumulative mean has a downward trend when the simulation ends. It is possible that running this case for longer would result in a closer match with the experimental data. However, we did not run this any further to be consistent with the other results. Increasing the simulation time is equivalent in some sense to obtaining a more refined solution.

The cumulative means for lower angle of attack cases flatten out quickly. This is because the flow is steady. We now further analyze the time histories to formalize the difference between steady and unsteady conditions. The time histories for steady and unsteady conditions have distinct characteristics. Steady time histories are nearly periodic and oscillate about the steady-state solution at a high frequency. Conversely, unsteady time histories are not periodic and have lower frequency content. Based on these observations, we can formulate a steadiness metric as a product of the periodicity and the dominant frequency of the time series. Using Fisher's g statistic [34, 35] as an estimate for the periodicity and nondimensionalizing the frequency, we define the steadiness metric (SM) as

$$\text{SM} = \frac{\max\limits_{i} P_i}{\sum\limits_{i} P_i} \frac{f_{P_{\max}} L_{\text{ref}}}{U_\infty}, \tag{1}$$

where P_i represents the periodogram of the time series and $f_{P_{\max}}$ is the frequency associated with the peak of the periodogram. We plot the steadiness metric for the 24M DDES results in Fig. 12. The steadiness metric is high from 0 to 20 deg, indicating that the flow is steady. This corresponds exactly to the regime where RANS is accurate. The steadiness metric drops off above 20 deg, indicating that the flow is unsteady. The flow regimes identified using the steadiness metric are consistent with the regimes described by Hummel [36] for a 65 deg delta wing.


(a) Time histories
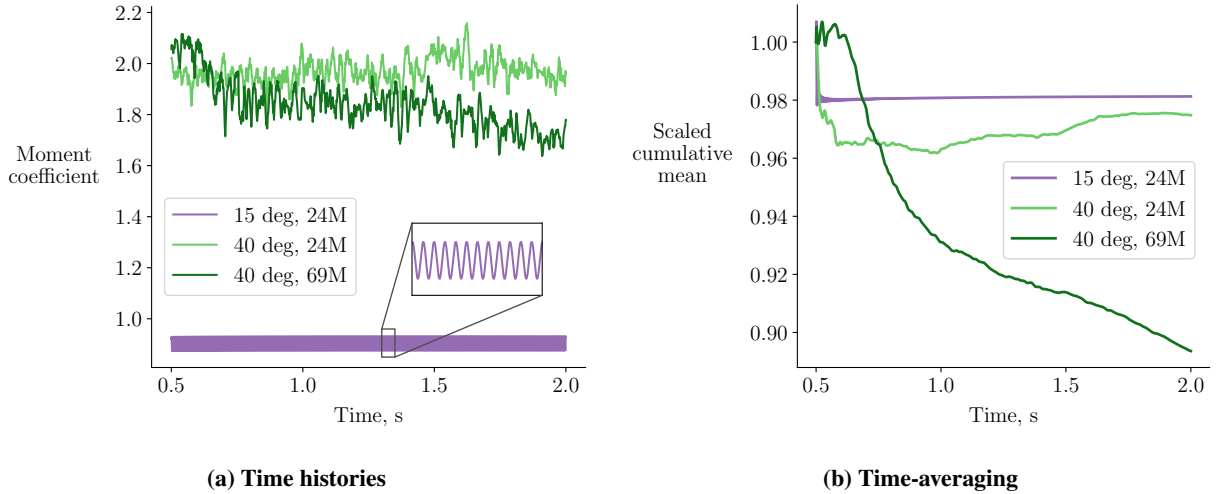
(b) Time-averaging

Fig. 11 DDES time histories are time-averaged to obtain coefficient values

V. Conclusions

In this work, we consider the flow over a delta wing with an aspect ratio of 2 at low-speed, high angle of attack conditions. We evaluate the accuracy of RANS and DDES at predicting force and moment coefficients for angles of attack from 0 to 40 deg. RANS provides accurate results for angles of attack up to 20 deg. We formulate a steadiness metric using the DDES results to show that this corresponds to the steady flow regime. RANS is inaccurate at higher angles of attack where the flow is unsteady. The lift and drag in this regime are underpredicted, and the pitching moment trend is incorrect.

DDES is more accurate than RANS at higher angles of attack. The errors in the lift and drag are within 6% for DDES compared to 20% for RANS. The DDES results are most sensitive to mesh refinement at the highest angles of attack. At 40 deg, the 69M mesh provides a much closer match with the experimental data than the 24M mesh, especially for the pitching moment. However, the break in the pitching moment is not fully captured even with the 69M mesh. The computational cost of DDES is 100–1000 times that of RANS.
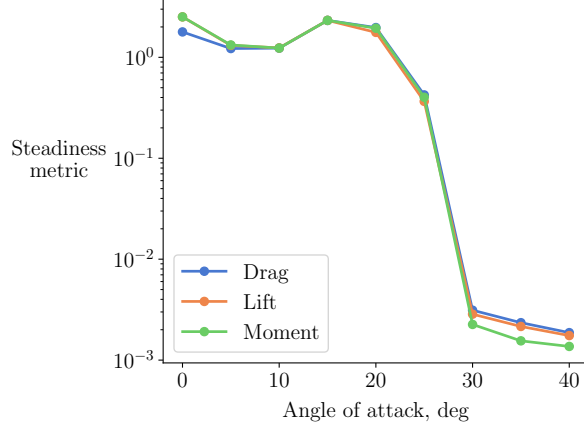
Fig. 12   The flow is steady up to $\alpha = 20°$

The predicted coefficients could be improved by using high-order schemes. High-order wall-modeled large eddy simulations (WMLES) have been used to accurately capture pitch break for the NASA Common Research Model at transonic conditions [37]. However, WMLES is even more costly than DDES. The ideal solver is both accurate and fast enough to be used in an iterative design or optimization procedure. RANS satisfies these requirements up to moderate angles of attack, but predicting high angle of attack characteristics at a computational cost suitable for iterative design remains a challenge.
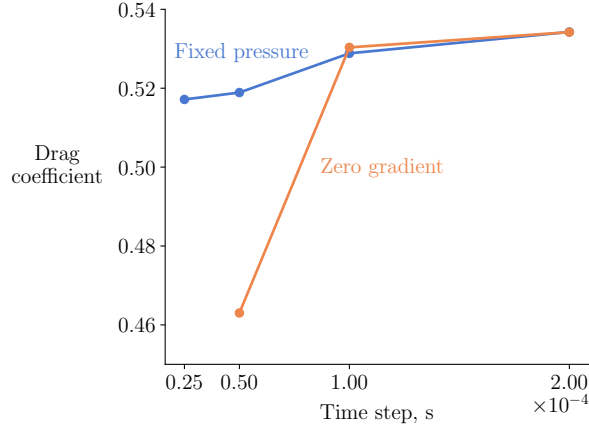
Fig. 13   Zero gradient pressure boundary conditions cause instabilities for small time steps

Appendix: pimpleFoam Instabilities

We find that time step convergence for pimpleFoam depends on the choice of farfield pressure boundary condition. Using a zero gradient boundary condition results in unstable solutions as the time step is decreased, shown by the nonphysical jump in the drag coefficient in Fig. 13. The coefficients converge using a fixed pressure boundary condition, which is what we use for all other DDES results in this work. The instabilities are a result of how the pressure Poisson equation is solved. The Poisson equation is ill-posed if all boundaries have Neumann boundary conditions [38]. If a solution exists, the solution plus a constant is also a solution. In such a case, OpenFOAM uses a reference pressure approach, which avoids nonunique solutions by fixing the pressure at one cell in the domain. When the time step is large, this works well and the coefficients are identical to the fixed pressure case. However, the reference pressure implementation in OpenFOAM makes the pressure equation ill-conditioned as the time step is refined. The details

of the implementation are peripheral to the current investigation, but we mention it here as a possible pitfall when using incompressible solvers in OpenFOAM. The version of OpenFOAM we use is OpenFOAM 7, released by the OpenFOAM Foundation.

Acknowledgments

References

[1] Luckring, J. M., "The discovery and prediction of vortex flow aerodynamics," *The Aeronautical Journal*, Vol. 123, No. 1264, 2019, p. 729–804. doi:10.1017/aer.2019.43.

[2] Torenbeek, E., *Essentials of Supersonic Commercial Aircraft Conceptual Design*, John Wiley & Sons Ltd., 2020.

[3] Nelson, C. P., "Effects of Wing Planform on HSCT Off-design Aerodynamics," *Proceedings of the 10th Applied Aerodynamics Conference*, 1992. doi:10.2514/6.1992-2629.

[4] Lan, C., and Hsu, C., "Effects of vortex breakdown on longitudinal and lateral-directional aerodynamics of slender wings by the suction analogy," *9th Atmospheric Flight Mechanics Conference*, 1982. doi:10.2514/6.1982-1385.

[5] Carlson, H. W., and Walkley, K. B., "A Computer Program for Wing Subsonic Aerodynamic Performance Estimates Including Attainable Thrust and Vortex Lift Effects," Tech. Rep. NASA CR 3515, NASA, Langley Research Center, Hampton, VA, 1982.

[6] Benoliel, A. M., and Mason, W. H., "Pitch-up characteristics for HSCT class planforms: Survey and estimation," *12th Applied Aerodynamics Conference*, 1994. doi:10.2514/6.1994-1819.

[7] Polhamus, E. C., "Predictions of vortex-lift characteristics by a leading-edge suction analogy," *Journal of Aircraft*, Vol. 8, No. 4, 1971, pp. 193–199. doi:10.2514/3.44254.

[8] Kulfan, R. M., "Wing Airfoil Shape Effects on the Development of Leading Edge Vortices," *5th Atmospheric Flight Mechanics Conference for Future Space Systems*, 1979. doi:10.2514/6.1979-1675.

[9] Kulfan, R. M., "Wing Geometry Effects on Leading Edge Vortices," *Aircraft Systems and Technology Meeting*, 1979. doi:10.2514/6.1979-1872.

[10] Mitchell, A. M., Barberis, D., Molton, P., and Délery, J., "Oscillation of Vortex Breakdown Location and Blowing Control of Time-Averaged Location," *AIAA Journal*, Vol. 38, No. 5, 2000, pp. 793–803. doi:10.2514/2.1059.

[11] Soemarwoto, B. I., and Boelens, O. J., "Simulation of vortical flow over a slender delta wing experiencing vortex breakdown," Tech. Rep. NLR-TP-2003-396, NLR, Netherlands, 2003.

[12] Görtz, S., "Detached-Eddy Simulations of a Full-Span Delta Wing at High Incidence," *21st Applied Aerodynamics Conference*, 2003. doi:10.2514/6.2003-4216.

[13] Morton, S., "Detached-Eddy Simulations of Vortex Breakdown over a 70-Degree Delta Wing," *Journal of Aircraft*, Vol. 46, No. 3, 2009, pp. 746–755. doi:10.2514/1.4659.

[14] Rizzi, A., and Luckring, J. M., "What Was Learned in Predicting Slender Airframe Aerodynamics with the F-16XL Aircraft," *Journal of Aircraft*, Vol. 54, No. 2, 2017, pp. 444–455. doi:10.2514/1.C033569.

[15] Lofthouse, A. J., and Cummings, R. M., "Numerical Simulations of the F-16XL at Flight-Test Conditions Using Delayed Detached-Eddy Simulation," *Journal of Aircraft*, Vol. 54, No. 6, 2017, pp. 2077–2099. doi:10.2514/1.C034045.

[16] Tomac, M., Jirasek, A., and Rizzi, A., "Hybrid Reynolds-Averaged Navier-Stokes/Large-Eddy Simulations of F-16XL in Low-Speed High-Alpha Flight," *Journal of Aircraft*, Vol. 54, No. 6, 2017, pp. 2070–2076. doi:10.2514/1.C034283.

[17] Forsythe, J. R., Squires, K. D., Wurtzler, K. E., and Spalart, P. R., "Detached-Eddy Simulation of the F-15E at High Alpha," *Journal of Aircraft*, Vol. 41, No. 2, 2004, pp. 193–200. doi:10.2514/1.2111.

[18] Cummings, R. M., and Schütte, A., "Detached-Eddy Simulation of the vortical flow field about the VFE-2 delta wing," *Aerospace Science and Technology*, Vol. 24, No. 1, 2013, p. 66–76. doi:10.1016/j.ast.2012.02.007.

[19] Jeans, T. L., McDaniel, D. R., Cummings, R. M., and Mason, W. H., "Aerodynamic Analysis of a Generic Fighter Using Delayed Detached-Eddy Simulation," *Journal of Aircraft*, Vol. 46, No. 4, 2009, pp. 1326–1339. doi:10.2514/1.40955.

[20] Rumsey, C. L., Slotnick, J. P., and Sclafani, A. J., "Overview and Summary of the Third AIAA High Lift Prediction Workshop," *Journal of Aircraft*, Vol. 56, No. 2, 2019, pp. 621–644. doi:10.2514/1.C034940.

[21] Jarrah, M. A., and Ashley, H., "Impact of flow unsteadiness on maneuvers and loads of agile aircraft," *30th Structures, Structural Dynamics and Materials Conference*, 1989. doi:10.2514/6.1989-1282.

[22] Mader, C. A., Kenway, G. K. W., Yildirim, A., and Martins, J. R. R. A., "ADflow: An open-source computational fluid dynamics solver for aerodynamic and multidisciplinary optimization," *Journal of Aerospace Information Systems*, Vol. 17, No. 9, 2020, pp. 508–527. doi:10.2514/1.I010796.

[23] Spalart, P., and Allmaras, S., "A One-Equation Turbulence Model for Aerodynamic Flows," *La Recherche Aerospatiale*, Vol. 1, 1994, pp. 5–21.

[24] Jameson, A., Schmidt, W., and Turkel, E., "Numerical Solution of the Euler Equations by Finite Volume Methods Using Runge–Kutta Time Stepping Schemes," *14th Fluid and Plasma Dynamics Conference*, 1981. doi:10.2514/6.1981-1259.

[25] Yildirim, A., Kenway, G. K. W., Mader, C. A., and Martins, J. R. R. A., "A Jacobian-free approximate Newton–Krylov startup strategy for RANS simulations," *Journal of Computational Physics*, Vol. 397, 2019, p. 108741. doi:10.1016/j.jcp.2019.06.018.

[26] Secco, N., Kenway, G. K. W., He, P., Mader, C. A., and Martins, J. R. R. A., "Efficient Mesh Generation and Deformation for Aerodynamic Shape Optimization," *AIAA Journal*, Vol. 59, No. 4, 2021, pp. 1151–1168. doi:10.2514/1.J059491.

[27] Chan, W. M., and Steger, J. L., "Enhancements of a three-dimensional hyperbolic grid generation scheme," *Applied Mathematics and Computation*, Vol. 51, No. 2–3, 1992, pp. 181–205. doi:10.1016/0096-3003(92)90073-A.

[28] Kenway, G. K. W., Secco, N., Martins, J. R. R. A., Mishra, A., and Duraisamy, K., "An Efficient Parallel Overset Method for Aerodynamic Shape Optimization," *Proceedings of the 58th AIAA/ASCE/AHS/ASC Structures, Structural Dynamics, and Materials Conference, AIAA SciTech Forum*, Grapevine, TX, 2017. doi:10.2514/6.2017-0357.

[29] Weller, H. G., Tabor, G., Jasak, H., and Fureby, C., "A tensorial approach to computational continuum mechanics using object-oriented techniques," *Computers in Physics*, Vol. 12, No. 6, 1998, pp. 620–631. doi:10.1063/1.168744.

[30] Spalart, P. R., Deck, S., Shur, M. L., Squires, K. D., Strelets, M. K., and Travin, A., "A New Version of Detached-eddy Simulation, Resistant to Ambiguous Grid Densities," *Theoretical and Computational Fluid Dynamics*, Vol. 20, No. 3, 2006, pp. 181–195. doi:10.1007/s00162-006-0015-0.

[31] Warming, R., and Beam, R. M., "Upwind second-order difference schemes and applications in aerodynamic flows," *AIAA Journal*, Vol. 14, No. 9, 1976, pp. 1241–1249.

[32] Issa, R. I., "Solution of the implicitly discretised fluid flow equations by operator-splitting," *Journal of Computational Physics*, Vol. 62, No. 1, 1986, pp. 40–65.

[33] Ashton, N., West, A., Lardeau, S., and Revell, A., "Assessment of RANS and DES methods for realistic automotive models," *Computers & Fluids*, Vol. 128, 2016, pp. 1–15. doi:10.1016/j.compfluid.2016.01.008.

[34] Fisher, R. A., "Tests of significance in harmonic analysis," *Proceedings of the Royal Society of London A*, Vol. 125, No. 796, 1929, pp. 54–59. doi:10.1098/rspa.1929.0151.

[35] Quinn, B. G., "Fisher's g Revisited," *International Statistical Review*, 2021. doi:10.1111/insr.12437.

[36] Hummel, D. J., "The International Vortex Flow Experiment 2 (VFE-2): Background, objectives and organization," *Aerospace Science and Technology*, Vol. 24, No. 1, 2013, pp. 1–9. doi:10.1016/j.ast.2012.08.008.

[37] Ghate, A. S., Kenway, G. K., Stich, G.-D., Browne, O. M. F., Housman, J. A., and Kiris, C. C., "Transonic Lift and Drag Predictions using Wall Modelled Large Eddy Simulations," *AIAA Scitech 2021 Forum*, 2021. doi:10.2514/6.2021-1439.

[38] LeVeque, R. J., *Finite Difference Methods for Ordinary and Partial Differential Equations*, Society for Industrial and Applied Mathematics, 2007.